catalysts

MDPI

Article

Synergistic Effect of Neighboring Fe and Cu Cation Sites Boosts Fe_nCu_m-BEA Activity for the Continuous Direct Oxidation of Methane to Methanol

Yan Li [1], Ning Liu [2,*], Chengna Dai [2], Ruinian Xu [2], Gangqiang Yu [2], Ning Wang [2], Jie Zhang [1] and Biaohua Chen [2,3]

[1] State Key Laboratory of Chemical Resource Engineering, Beijing University of Chemical Technology, Beijing 100029, China; ly1@buct.edu.cn (Y.L.); zhangjie@mail.buct.edu.cn (J.Z.)
[2] Faculty of Environment and Life, Beijing University of Technology, Beijing 100124, China; daicn@bjut.edu.cn (C.D.); xuruinian@bjut.edu.cn (R.X.); yugq@bjut.edu.cn (G.Y.); ning.wang.1@bjut.edu.cn (N.W.); chenbh@bjut.edu.cn (B.C.)
[3] Jiangsu Key Laboratory of Advanced Catalytic Materials and Technology, School of Petrochemical Engineering, Changzhou University, Changzhou 213164, China
* Correspondence: liuning@bjut.edu.cn

Abstract: Direct oxidation of methane to methanol (DMTM), constituting a major challenge for C_1 chemistry, has aroused significant interest. The present work reports the synergistic effect of neighboring [Fe]–[Cu] cations, which can significantly boost the CH_3OH productivity (100.9 and 41.9 → 259.1 $\mu mol \cdot g^{-1}_{cat} \cdot h^{-1}$) and selectivity (0.28 and 17.6% → 71.7%) of the best performing $Fe_{0.6\%}Cu_{0.68\%}$-BEA (relative to monomeric $Fe_{1.28\%}$- and $Cu_{1.28\%}$-BEA) during the continuous H_2O-mediated N_2O DMTM. The combined experimental (in situ FTIR, D_2O isotopic tracer technique) and theoretical (DFT, ab initio molecular dynamics (AIMD)) studies reveal deeper mechanistic insights that the synergistic effect of [Fe]–[Cu] can not only significantly favor active O production (ΔG = 0.18 eV), but also efficiently motivate the reaction following a H_2O proton-transfer route (ΔG = 0.07 eV), eventually strikingly promoting CH_3OH productivity/selectivity. Generally, the proposed strategy by employing the synergistic effect of bimetallic cations to modify DMTM activity would substantially favor other highly efficient catalyst designs.

Keywords: methane direct oxidation to methanol (DMTM); N_2O; $[Fe\text{-}O\text{-}Cu]^{2+}$ active site; mechanism; ab initio molecular dynamics (AIMD)

Citation: Li, Y.; Liu, N.; Dai, C.; Xu, R.; Yu, G.; Wang, N.; Zhang, J.; Chen, B. Synergistic Effect of Neighboring Fe and Cu Cation Sites Boosts Fe_nCu_m-BEA Activity for the Continuous Direct Oxidation of Methane to Methanol. *Catalysts* **2021**, *11*, 1444. https://doi.org/10.3390/catal11121444

Academic Editors: Vincenzo Vaiano and Olga Sacco

Received: 5 November 2021
Accepted: 25 November 2021
Published: 27 November 2021

1. Introduction

Methane, being a primary component of natural gas, constitutes the main feedstock during methanol production, which traditionally follows the syngas route, needing high temperature and pressure [1]. By contrast, the direct oxidation of methane to methanol (DMTM) operated under mild conditions is greatly appealing for CH_3OH production; however, this process suffers from low selectivity and productivity, due to the extremely high C-H bond energy (413 $kJ \cdot mol^{-1}$) of CH_4 but relatively low thermostability of CH_3OH [2–4]. Although it is still a major challenge to make breakthroughs for the DMTM, the development of suitable catalysts and reaction systems to promote CH_3OH selectivity and productivity has never ceased.

Methane monooxygenases (MMOs), as a type of methanotrophic bacteria, can readily transform CH_4 into CH_3OH at room temperature, the active site of which consists of iron or copper [5]. To mimic its catalytic behavior, the Fe- and Cu-exchanged zeolites have been extensively investigated for the DMTM [6–16], wherein the specific active site motifs significantly affect the DMTM activity. For example, Jeong et al. [7] recently reported a continuous DMTM by passing O_2 over Cu-MOR, finding that the binuclear $[Cu\text{-}O\text{-}Cu]^{2+}$ site possessed much higher activity than that of the mononuclear $[Cu]^+$ site. To further

improve the DMTM activity, the strategy of introducing another transition metal into the Cu- or Fe-exchanged zeolite to modify the active motif has also been proposed [8–14]. The group of Hutchings [8–10] performed pioneering works finding that the Cu species can dramatically promote the CH_3OH selectivity (>92%) and productivity of the Fe/Cu-ZSM-5 zeolite catalyst through efficiently inhibiting the overoxidation of CH_3OH (into formic acid and CO_2) during the H_2O_2 DMTM. Recently, Yu et al. [11] further found that the Cu species of Fe/Cu-ZSM can also facilitate the generation of OH- radicals which thereby can quickly react with -CH_3 to produce CH_3OH. Meanwhile, some theoretical simulations have also been conducted for the DMTM over a series of zeolitic bimetal active centers of $[Cu\text{-}O\text{-}M]^{2+}$ and $[Cu\text{-}O_2\text{-}M]^{2+}$ (M = Pd, Pt, Fe, Co, Ni, Zn, Au and Ag) [12–14], aiming at favoring the rational design of highly efficient bimetallic ion-exchanged zeolite catalysts.

In addition to the active site motifs, the utilized oxidant as well as H_2O also significantly affect the zeolitic DMTM activity and efficiency. In comparison to O_2 and H_2O_2, N_2O is a promising oxidant for the DMTM due to the much more ready formation of highly active oxygen species (named αO, T < 250 °C) after the in situ interaction with the metal modified zeolite (M-Z) catalyst [17]. Additionally, the in situ generation of active oxygen (αO) at low temperatures demonstrates N_2O as being a promising oxidant for the continuous DMTM, which can strikingly promote DMTM efficiency relative to that of the widely reported stepwise DMTM. Moreover, differing from H_2O_2, which is a type of expensive oxidant, N_2O can be largely released from the tail gas of the adipic acid industry (effluent N_2O content > 35 vol%) [18], which can effectively solve the source problem of N_2O for the N_2O DMTM. In light of these advantages, several studies on N_2O DMTM operated under moderate temperatures have recently been reported, achieving the superior DMTM activity relative to that of O_2 DMTM [19–25]. As for H_2O, it has long been recognized as a solvent to sweep out CH_3OH during the DMTM [6,26] until recently, when Bokhoven et al. [27,28] and Liu et al. [29] discovered that H_2O could directly participate in the DMTM, working as an oxidant and directing the reaction pathway. Inspired by these literature reports, a proton-transfer reaction of H_2O can be found in our previous work [24], pronouncedly the enhancing of CH_3OH production (16.8 (absence of H_2O) → 242.9 $\mu mol \cdot g^{-1}_{cat} \cdot h^{-1}$) and the selectivity (3.1 → 71.6%) of $Cu_{0.6\%}$-BETA (BEA) zeolite during the continuous N_2O DMTM.

In the present work, to further improve the catalytic behavior of $Cu_{0.6\%}$-BEA, a series of bimetallic Fe_nCu_m-BEA zeolites with different Fe/Cu ratios (see Table S1) was prepared and evaluated for the H_2O-mediated continuous N_2O DMTM, based on the acknowledgement that the Fe-modified zeolite is much more favorable for N_2O dissociation [17], as well as the assumption that the bimetallic Fe and Cu can provide some unique activity through the synergetic effect. In particular, a strikingly promoted activity can be observed for the best-performing sample of $Fe_{0.6\%}Cu_{0.68\%}$-BEA. Specifically, higher CH_3OH productivity (259.1 $\mu mol \cdot g^{-1}_{cat} \cdot h^{-1}$) can be achieved at a much lower reaction temperature (T = 270 °C) relative to that of $Cu_{0.6\%}$-BEA (242.9 $\mu mol \cdot g^{-1}_{cat} \cdot h^{-1}$, T = 320 °C), while in comparison to the monomeric $Fe_{1.28\%}$- or $Cu_{1.28\%}$-BEA with the same metal loadings, $Fe_{0.6\%}Cu_{0.68\%}$-BEA also exhibits overwhelming superiority in both CH_3OH productivity (259.1 versus 100.9 and 41.9 $\mu mol \cdot g^{-1}_{cat} \cdot h^{-1}$) and CH_3OH selectivity (71.7% versus 0.28 and 17.6%). These can be closely correlated with the synergetic effect of the neighboring [Fe]–[Cu] cations, which can efficiently favor the active O generation as well as the H_2O-mediated proton-transfer reaction. This specific mechanistic insight was illustrated based on the combined experimental (in situ DRIFTS and TPD-MS) and theoretical (DFT and ab initio dynamics (AIMD)) investigations. Overall, the present work systematically investigated reported the synergistic effect of the neighboring [Fe]–[Cu] cations over the Fe_nCu_m-BEA zeolite, eventually leading to boosted H_2O-mediated N_2O DMTM activity, the study of which would substantially contribute to other highly efficient zeolite catalyst designs for the continuous DMTM.

2. Result and Discussion

2.1. Physicochemical Property Characterizations

Table S1 lists the physiochemical properties of the investigated Fe_nCu_m-BEA samples (n and m represent the metal loadings), which were prepared by the tradition ion-exchange method. Briefly, the H-BEA (5g) was mixed with certain amounts (see Table S2) of $Fe(NO_3)_3{\cdot}9H_2O$ and $Cu(NO_3)_2{\cdot}5H_2O$ and thereby solved by 200 mL deionized water under stirring for 4 h at 100 °C. After being washed, dried (100 °C, 24 h) and calcined (550 °C, 4 h), the final product can be obtained. As noted, for the purpose of comparison the physiochemical properties of the monomeric $Fe_{1.28\%}$- and $Cu_{1.28\%}$-BEA, being prepared by the incipient-wetness impregnation method and with a metal loading amount of 1.28 wt.% (see details in Supplementary Materials), was also listed in Table S1. The small crystallite size (~17–18 mm) associated with a high Brunner−Emmet−Teller (BET) surface area (>500 $m^2{\cdot}g^{-1}$) indicates the nano-zeolite catalysts of the prepared Fe_nCu_m-BEA and H-BEA. The related XRD patterns confirm the characteristic BEA crystal structures of the prepared samples, with no CuO_x or Fe_xO_y diffraction patterns being observed (see Figure S2a). However, the coexistence of well-dispersed metal oxides cannot be totally ruled out due to their minor amounts, being below the XRD detection limit.

To further identify the chemical states of the loaded Fe and Cu species over the Fe_nCu_m-BEA samples, the H_2 temperature program reduction (H_2-TPR) was thereby conducted, with the results being profiled in Figure 1a. As can be seen, there are four types of reduction peak in total, as marked by orange, purple, dark green and blue, which can be assigned to be the reduction of CuO, Fe^{3+} ion, Cu^{2+} ions and Fe_xO_y, respectively [18,24,30]. The species occupations are further depicted in Figure 1b (see details in Table S3), indicating that the Cu^{2+} cations constitute the major species over $Fe_{0.38\%}Cu_{0.74\%}$, while both the Cu^{2+} and Fe^{3+} cations can be observed for $Fe_{0.6\%}Cu_{0.68\%}$-BEA (0.56 and 0.40%) and $Fe_{1.0\%}Cu_{0.5\%}$-BEA (0.37 and 0.28%), although large amounts of Fe_xO_y species (0.74%, Figure 1b) can also coexist with metal cations over $Fe_{1.0\%}Cu_{0.5\%}$-BEA. Noteworthily, the Cu^{2+} cations' contents (green columns) were higher than those of the Fe^{3+} cations (purple columns), even for the sample of $Fe_{1.0\%}Cu_{0.5\%}$-BEA (0.37 versus 0.28%, Figure 1b) with much higher Fe loadings than those of Cu. This finding reveals that the Cu^{2+} cations prefer to occupy the Brönsted acid ion-exchange site compared to Fe^{3+} cations, eventually resulting in Fe_xO_y as the major Fe species, especially for the sample of $Fe_{1.0\%}Cu_{0.5\%}$-BEA with the highest Fe loadings. The valance states of the loaded Cu and Fe species of Fe_nCu_m-BEA were further characterized by XPS, as shown in Figure 1c,d. The main peak located at 933.5 (Cu $2p_{3/2}$), being associated with a shake-up peak at 944.5 eV (Figure 1c), indicates the characteristic Cu^{2+} valance state of the surface Cu species [18], while the two main peaks located at 712.3 (Fe $2p_{3/2}$) and 725.7 eV (Fe $2p_{1/2}$), being associated with the satellite peaks at 718.2 and 732.9 eV (Figure 1d), indicate the 3+ valance state of the surface Fe species [31]. For comparison, H_2-TPR and XPS were also conducted on the monomeric $Fe_{1.28\%}$ and $Cu_{1.28\%}$-BEA (see Figure 1a and Figure S3a,b), which indicate that both the CuO (0.52%) and Cu^{2+} (0.76%) cations can be formed over $Cu_{1.28\%}$-BEA. The large reduction domain of Fe^{3+} species over Fe-BEA-1.28% (250–600 °C of Figure 1a) can be related to the reduction of Fe^{3+} cations or oxo-cations into Fe^{2+},[18] which can be further confirmed by the H_2 consumption quantitation (see Table S3). As noted, in comparison to that of Fe-BEA-1.28%, the Fe^{3+} cation reduction peaks became narrower for the scenario of Fe_nCu_m-BEA samples, which can be related to the much lower Fe^{3+} cation amounts resulting from the much stronger ion-exchange ability of Cu^{2+} cations at the Brönsted acid site (as stated above).

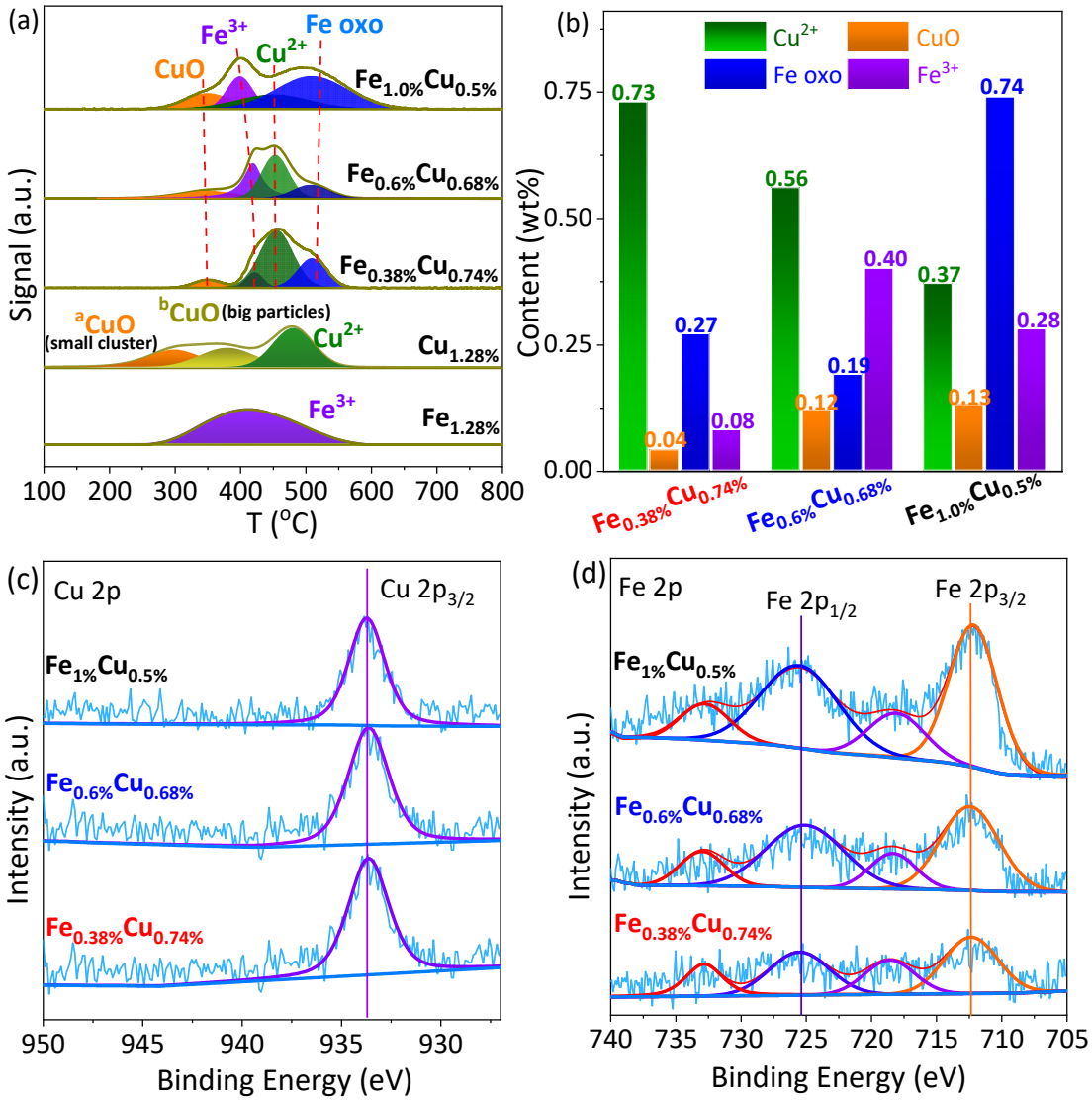

Figure 1. (**a**) H_2-TPR profiles of the investigated Fe_nCu_m-BEA samples; (**b**) Fe, Cu species quantification based on the H_2 consumption of H_2-TPR; XPS of Cu 2p; (**c**) and Fe 2p; (**d**) of the Fe_nCu_m-BEA samples.

2.2. Activity Measurement

2.2.1. Activity Comparison with Monomeric Fe- and Cu-BEA

With a basic understanding of the loaded metallic species, the continuous N_2O DMTM activity measurements were further conducted over the Fe_nCu_m-BEA and $Fe_{1.28\%}$- $Cu_{1.28\%}$-BEA samples, as shown in Figure 2a–d and Figure S4, being associated with the CH_4 conversion and product selectivities being listed in Table S4. As can be seen, much higher CH_3OH productivities (Figure 2a) and selectivities (Figure 2b & Table S4) can be observed for the samples of Fe_nCu_m-BEA relative to those of the monomeric $Fe_{1.28\%}$- and $Cu_{1.28\%}$-BEA. Especially for the best-performed sample of $Fe_{0.6\%}Cu_{0.68\%}$-BEA, it displays a boosted CH_3OH productivity (259.1 $\mu mol \cdot g^{-1}_{cat} \cdot h^{-1}$, Figure 2a), being respectively of 2.6 and 6.2 times high than those of $Fe_{1.28\%}$- and $Cu_{1.28\%}$-BEA (100.9 and 41.9 $\mu mol \cdot g^{-1}_{cat} \cdot h^{-1}$) with the similar total metal loadings. This finding implies that there probably exists some synergetic effect between the loaded Fe and Cu species, which can efficiently promote the H_2O-mediated N_2O DMTM activity of $Fe_{0.6\%}Cu_{0.68\%}$-BEA. This will be further discussed later based on the combined experimental and theoretical studies. As for the monomeric $Fe_{1.28\%}$-BEA, large amounts of CO_2 (selectivity of 97.2%, see Figure 2b) can be formed, being accompanied with the N_2O conversion of 99.1% and CH_4 conversion of 47.8%,

which indicates the overoxidation of CH_4 probably due to the strong oxidation property of the generated αO over the Fe cation site; additionally, the $Cu_{1.28\%}$-BEA displays the lowest CH_3OH productivity (41.9 $\mu mol \cdot g^{-1}_{cat} \cdot h^{-1}$), which can be related to the lower reaction efficiency to generate αO of the Cu cations relative to that of Fe as well as the coexistence of large amounts of CuO_x species (0.52%, see Table S3) that can readily lead to the overoxidation of CH_3OH into CO_2 (22.6%, Figure 2b).

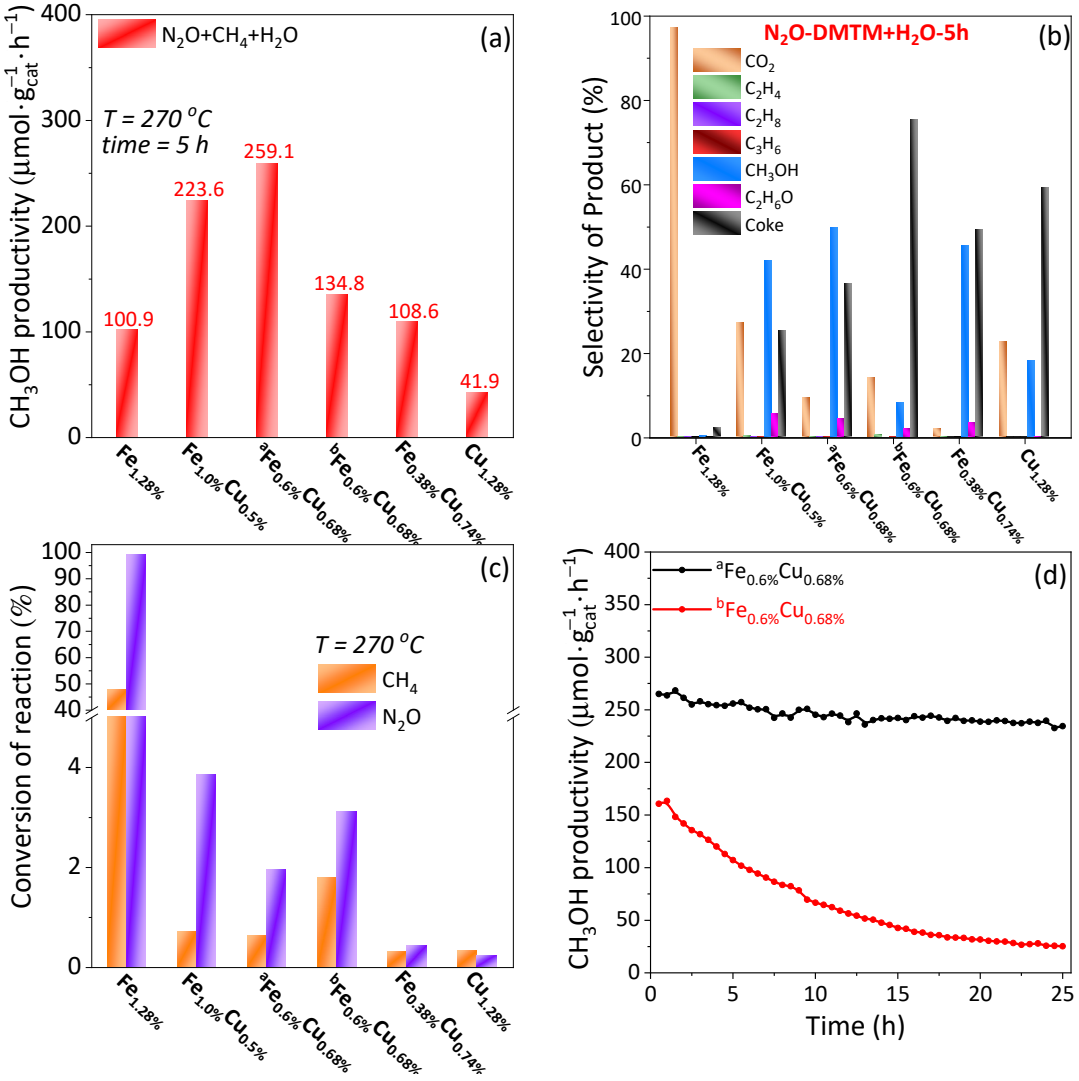

Figure 2. Activity measurement results of H_2O-mediated continuous N_2O DMTM over Fe_nCu_m-BEA and $Cu_{1.28\%}$- and $Fe_{1.28\%}$-BEA; as noted, for the purpose of better description, the activity measurement results for the sample of $Fe_{0.6\%}Cu_{0.68\%}$-BEA evaluated in both scenarios of presence ($^aFe_{0.6\%}Cu_{0.68\%}$) and absence of H_2O ($^bFe_{0.6\%}Cu_{0.68\%}$) are depicted in Figure 2: (**a**) CH3OH productivity derived as an average value after a 5 h reaction; (**b**) product selectivity; the selectivities for the $Fe_{0.6\%}Cu_{0.68\%}$-BEA samples were derived from 25 h of activity measurement; (**c**) reactant conversion of CH_4 and N_2O; (**d**) 25 h long-term activity test; reaction conditions: N_2O:CH_4:H_2O:He = 30:15:10:45, GHSV = 12,000 h^{-1}, T = 270 °C.

In addition to that, it can be found that the simultaneous introduction of 10 vol% H_2O into the reaction system can pronouncedly promote the CH_3OH productivity (134.8 $\mu mol \cdot g^{-1}_{cat} \cdot h^{-1}$ → 259.1 $\mu mol \cdot g^{-1}_{cat} \cdot h^{-1}$, Figure 2a) and CH_3OH selectivity (14.4 → 71.7%, Figure 2b) as well as the long-term stability (passing through 25 h's test, Figure 2d) of the best-performed $Fe_{0.6\%}Cu_{0.68\%}$-BEA. This finding gives us a clue that there probably also exits the proton-transfer reaction over the $Fe_{0.6\%}Cu_{0.68\%}$-BEA, wherein the H_2O molecule could directly participate in the reaction through a proton-transfer route, as proposed in our previous work over the $Cu_{0.6\%}$-BEA zeolite catalyst [24], eventually

pronouncedly promoting the CH_3OH productivity & selectivity. On the contrary, a large amount of coke can be generated during H_2O-absence N_2O DMTM over $Fe_{0.6}Cu_{0.68}$-BEA (67.3%, see Figure 2b), which can be closely related to the undesired side reaction of the accumulated CH_3^- radicals being generated during CH_4 activation over the active site. Meanwhile, it is also worth noting that the $Fe_{0.6\%}Cu_{0.68\%}$-BEA can achieve higher CH_3OH productivity under a much lower reaction temperature (259.1 $\mu mol \cdot g^{-1}_{cat} \cdot h^{-1}$, T = 270 °C) than that of $Cu_{0.6\%}$-BEA (242.5 $\mu mol \cdot g^{-1}_{cat} \cdot h^{-1}$, T = 320 °C) of our previous report [24], which can well verify the viability of the proposed strategy by modifying active site motifs to improve the N_2O DMTM activity of Cu-BEA.

2.2.2. Activity Comparison among Fe_nCu_m-BEA

The diverse catalytic activities of the Fe_nCu_m-BEA samples can be closely correlated with the chemical states as well as the correlated synergetic effect of the loaded Fe and Cu species. As is well known, the metal cations constitute the active sites for N_2O dissociation [17], which are responsible for the production of αO for the scenario of the present reaction system, while the metal oxides readily lead to the overoxidation of CH_3OH into CO_2 [24]. In this regard, we can deduce that the highest CH_3OH productivity of $Fe_{0.6\%}Cu_{0.68\%}$-BEA can be closely correlated with its higher Fe and Cu metal cation amounts (0.56 and 0.40%, Figure 1b), which greatly favor the active O production as well as the reaction synergies between these bimetal cations. Similar findings can also be derived for the sample of $Fe_{1.0\%}Cu_{0.5\%}$-BEA; however, the relatively lower metal cation amounts (0.37 and 0.28%, Figure 1b) combined with the larger amounts of coexisting Fe_xO_y (0.74%, Figure 1b) constitute two major factors leading to the relatively lower CH_3OH productivity compared to that of $Fe_{0.6\%}Cu_{0.68\%}$-BEA (223.6 versus 259.1 $\mu mol \cdot g^{-1}_{cat} \cdot h^{-1}$, Figure 2a). As for the sample of $Fe_{0.38\%}Cu_{0.74\%}$-BEA, possessing the highest Cu cation amount (0.73%, Figure 1b), it exhibits the lowest CH_3OH productivity (108.6 $\mu mol \cdot g^{-1}_{cat} \cdot h^{-1}$) among the Fe_nCu_m-BEA samples; this can be closely related to it having the lowest amount of Fe cations (0.08%, Figure 1b), which significantly limits the reaction synergies between the loaded Cu and Fe cations. This finding can also support the proposed assumption that the synergetic effect of the loaded Fe and Cu species (the metal cations) play a vital role in the H_2O-mediated N_2O DMTM.

2.3. Evolution of the Bimetal Active Center of [Fe-O-Cu] and Thermodynamics Stability Analysis

2.3.1. NO In Situ FTIR

The in situ FTIR utilizing NO as the probe molecule (NO in situ FTIR) was employed to explore the active-site structure evolutions under the reaction condition of the present work over the best-performed $Fe_{0.6\%}Cu_{0.68\%}$-BEA. As shown in Figure 3a, after the He (>99.999 vol%, T = 500 °C for 1 h) pretreatment (wine line), two broad v(NO) bands centered at 1873 and 1864 cm^{-1}, being associated with characteristic v(NO) bands belonging to the monomeric metal cation sites including 1962, 1937 and 1913 cm^{-1} of $[Cu]^{2+}$ and 1840, 1818, and 1805 cm^{-1} of reduced-cation sites ($[Cu]^+$ or $[Fe]^{2+}$) [32–34], can be clearly observed. Interestingly, after the further N_2O (30 vol% in He, T = 250 °C for 1 h) treatment, an obvious enhancement for the bands at 1873 and 1864 cm^{-1} (green line) can be clearly observed, wherein the band of 1864 cm^{-1} was merged as a shoulder of 1873 cm^{-1}, being accompanied with the evident decreasing of v(NO) over the monomeric cation sites, especially for the 1840, 1818, and 1805 cm^{-1} of reduced metal cation sites.

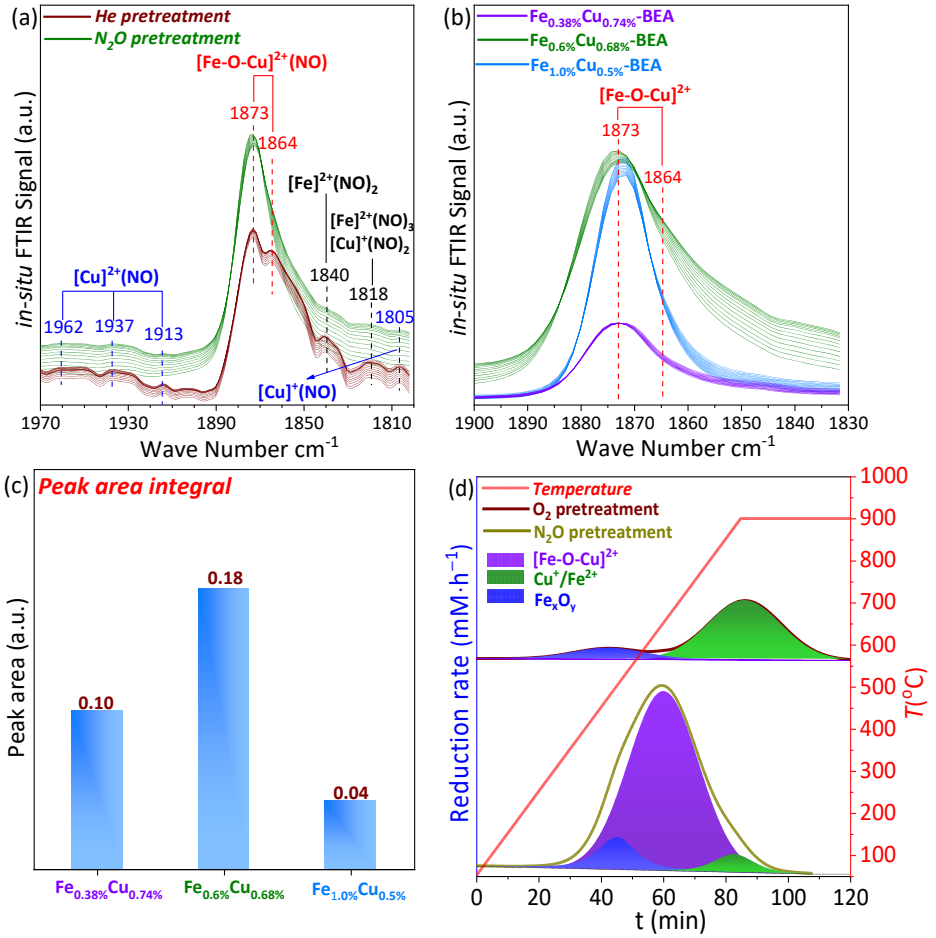

Figure 3. (**a**) In situ FTIR with NO as the probe molecule over $Fe_{0.6\%}Cu_{0.68\%}$-BEA after the in situ pretreatment by He (>99.999 vol%, 40 mL·min^{-1} at T = 500 °C for 1 h) and N_2O (30 vol% in He, 40 mL·min^{-1} at T = 250 °C for 1 h); as noted, during the N_2O pretreatment, the sample was also initially pretreated with He at 500 °C for 1 h and subsequently pretreated with N_2O; (**b**) NO in situ FTIR of the Fe_nCu_m-BEA samples after the N_2O pretreatment; (**c**) peak area comparisons of 1873 and 1864 cm^{-1} in panel (**b**) for the Fe_nCu_m-BEA samples; (**d**) H_2-TPR of $Fe_{0.6\%}Cu_{0.68\%}$-BEA after the O_2 and N_2O pretreatment; this specific pretreatment strategy is similar to that utilized during NO in situ FTIR.

After carefully analyzing this experimental phenomenon as well as scanning the literature reports [32–34], we would assign the major bands at 1873 and 1864 cm^{-1} to be v(NO) over the evolved bimetal [Fe-O-Cu] site, being in the form of [NO-Fe-O-Cu] and [Fe-O-Cu-NO]. Specifically, after the He pretreatment, part of the monomeric Fe^{3+} and Cu^{2+} cations would be auto-reduced by displaying the characteristic v(NO) bands at 1840, 1818 and 1805 cm^{-1}; concurrently, parts of the neighboring Fe^{3+} and Cu^{2+} cations would prefer forming the bimetallic [Fe-O-Cu] through the dihydroxylation by displaying tow-obvious NO adsorption bands at 1873 and 1864 cm^{-1} (see Figure 3a). The subsequent N_2O treatment would further favor [Fe-O-Cu] formation through the interaction with reduced neighboring Fe and Cu cations. The free energy barrier of this step was simulated to be only 0.18 eV at T = 270 °C (as will be further discussed later). In this regard, the further enhancements of v(NO) at 1873 and 1864 cm^{-1} ([Fe-O-Cu] site) being accompanied with the simultaneous decreasing of v(NO), especially at the reduced metal cation sites of (1840, 1818, 1805 cm^{-1}), can be observed in Figure 3a. To exclude the possibility of generations of large amounts of [Cu-O-Cu] or [Fe-O-Fe] species, the UV-vis and ab initio thermodynamics analyses have also been conducted (See Figure S5a,b): (i) no obvious characteristic UV-vis band belonging to [Cu-O-Cu] (~440 nm) can be observed in Figure S5a, although the same

formation Gibbs free energy ($\Delta_f G$ = −7.62 eV) can be achieved for the [Cu-O-Cu] and [Fe-O-Fe] site (see Figure S5b); (ii) the [Fe-O-Cu] exhibits much lower formation Gibbs free energy than that of [Fe-O-Fe] (−7.62 versus 7.15 eV, see Figure S5b), which indicates that it would be much more preferable to form [Fe-O-Cu] under the reaction condition of the present work due to the higher thermodynamic stabilities; (iii) the split two obvious v(NO) bands at 1873 and 1864 cm^{-1} (see Figure 3a of He pretreatment) can also give good evidence of the formation of $[Fe\text{-}O\text{-}Cu]^{2+}$ species due to the fact that the [Fe-O-Fe] can only show up one type of characteristic v(NO) band around 1875 cm^{-1} [32].

In light of the above statement, we can deduce that the [Fe-O-Cu] would constitute the major active site during the N_2O DMTM over $Fe_{0.6\%}Cu_{0.68\%}$-BEA by displaying much more extensive band intensities at 1873 and 1864 cm^{-1} than those of 1840, 1818 and 1805 cm^{-1} after the N_2O pretreatment (see Figure 3a). To make comparisons, the NO in situ FTIR was also conducted over $Fe_{0.38\%}Cu_{0.74\%}$- and $Fe_{1.0\%}Cu_{0.5\%}$-BEA (being after in situ N_2O pretreatment), as shown in Figure 3b. The characteristic v(NO) bands over the bimetallic [Fe-O-Cu] site (1873 and 1864 cm^{-1}) can also be clearly observed for these two samples, the band area of which were however much lower than that of $Fe_{0.6\%}Cu_{0.68\%}$-BEA, as quantified in Figure 3c. This finding gives us a clue that the much higher N_2O DMTM activity of $Fe_{0.6\%}Cu_{0.68\%}$-BEA (Figure 2a) can be closely correlated with its higher amounts of evolved [Fe-O-Cu] active species in comparison to other two samples.

2.3.2. H_2-TPR after N_2O and O_2 Pretreatment

The H_2-TPR was further conducted over the N_2O and O_2 (taken as a reference) pretreated $Fe_{0.6\%}Cu_{0.68\%}$-BEA to confirm the evolved [Fe-O-Cu] site. Similarly, a pretreatment strategy to that of NO in situ FTIR was applied, wherein the sample were initially pretreated by He at T = 500 °C for 1 h before the subsequent N_2O (30 vol% in He, T = 250 °C for 1 h) and O_2 (15 vol% in He, T = 500 °C for 1 h) pretreatments; and to obtain the better signals, the mass spectrometer (MS) was utilized to monitor the H_2 (m/e = 2) consumptions. As noted, the O_2 pretreatment temperature of 500 °C was chosen according to literature reports [26] that it commonly needs a high temperature (T > 500 °C) to generate active O species during DMTM over the zeolitic catalyst. As shown in Figure 3d, three types of H_2 reduction peaks can be clearly observed, which can be respectively corresponding to the reduction of Fe_xO_y (~500 °C, blue), [Fe-O-Cu] (650 °C, purple) and the Fe^{2+}/Cu^{+} cations (900 °C, dare green). Obviously, in comparison with the O_2-pretreated $Fe_{0.6\%}Cu_{0.68\%}$-BEA, much higher amounts of [Fe-O-Cu] species (purple peak) can be formed over the N_2O-pretreated $Fe_{0.6\%}Cu_{0.68\%}$-BEA, which also constitute the major active species being in good agreement with the NO in situ FTIR result of Figure 3a. On the contrary, only trace [Fe-O-Cu] can be formed over the $Fe_{0.6\%}Cu_{0.68\%}$-BEA due to the extremely low dissociation activity of O_2. This finding is in good agreement with the significantly lower O_2 DMTM activity (~1 $\mu mol \cdot g^{-1}{}_{cat} \cdot h^{-1}$ of CH_3OH, see Figure S6) relative to that of N_2O DMTM. Therefore, the evolution of the [Fe-O-Cu] site through the in situ interaction with N_2O at low temperature (T = 250 °C) can be safely confirmed based on the H_2-TPR of Figure 3d over the $Fe_{0.6\%}Cu_{0.68\%}$-BEA, which also constitutes the major active sites during N_2O DMTM over $Fe_{0.6\%}Cu_{0.68\%}$-BEA.

2.3.3. Ab Initio Thermodynamics (AIT) Analysis

In this section, DFT-based ab initio thermodynamics (AIT) analysis was further conducted to evaluate the thermostability of the [Fe-O-Cu] site under the reaction conditions of the present work (10 vol% H_2O, 30 vol% N_2O and 1atm), as shown in Figure 4b,c, wherein the other active-site motifs, including the monomeric [Cu], [Cu-O], [CuOH] and neighboring bimetallic [Fe]–[Cu] sites, were also taken into account. Obviously, the [Fe-O-Cu] site exhibited dramatically lower ΔG values than the other active sites, indicating the stronger thermodynamic stability of the evolved [Fe-O-Cu] site. As noted, the much higher thermodynamic stability of [Fe-O-Cu] relative to that of [Fe]–[Cu] indicates that it is also

thermodynamically favorable to evolve into [Fe-O-Cu] through the in situ interaction of [Fe]–[Cu] with N_2O under the reaction conditions of the present work.

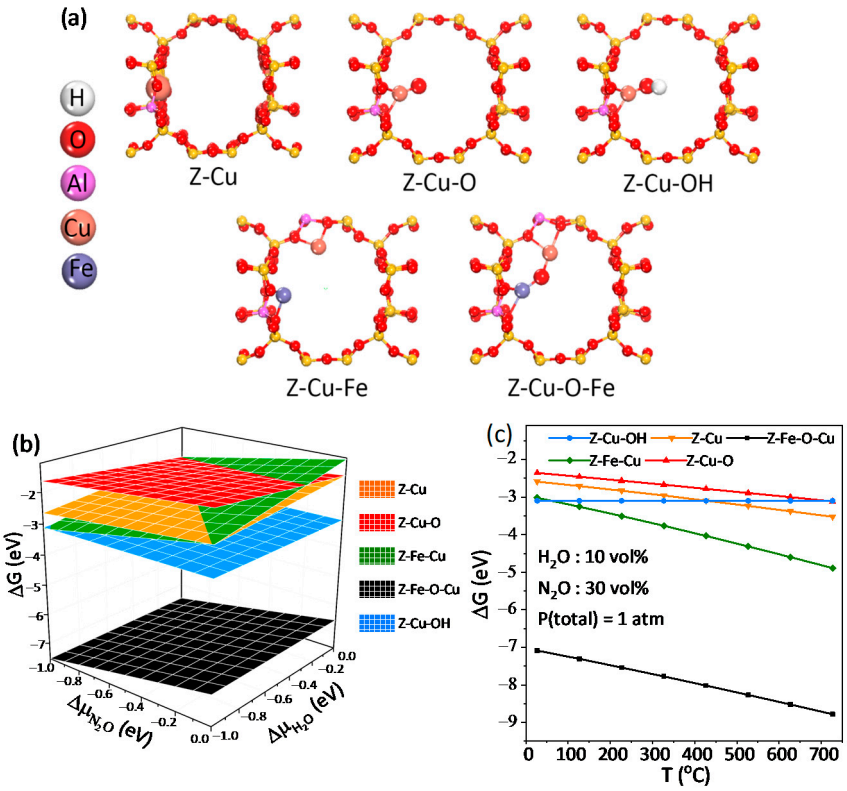

Figure 4. (**a**) Optimized structure models with diverse active-site motifs on the BEA zeolite; Z represents the BEA zeolite framework; the Al atom was located at the T5 site for the monomeric active site [18]; the T2 and T5 sites were chosen as the neighboring framework Al site based on previous studies [24]; (**b**) Gibbs-free energy of formation (ΔG) as a function of $\Delta\mu_{N2O}$ and $\Delta\mu_{H2O}$ (chemical potentials) for different active motifs at T = 270 °C; (**c**) ΔG as a function of temperature under N_2O DMTM reaction condition of 10 vol% H_2O, 30 vol% N_2O and 1 atm pressure.

2.4. Mechanistic Insight into Synergetic Effect of Neighboring Fe and Cu Cations during H_2O-Mediated N_2O DMTM

2.4.1. Experimental Mechanism Study

Based on the above studies, the active-site motif evolutions have been clarified. In this section, the H_2O-mediated N_2O DMTM reaction mechanism was further investigated by in situ FTIR and D_2O isotopic tracer techniques to explore the reaction synergy of the loaded neighboring Cu and Fe cations over the best-performing $Fe_{0.6\%}Cu_{0.64\%}$-BEA.

(a) In situ FTIR

As shown in Figure 5a, three types of $\nu(CH_x)$ vibration frequencies can be clearly observed after introducing the reactant mixtures (N_2O, CH_4 and H_2O) into the system at T = 270 °C, corresponding to the ν(CH) of CH_4 (3015 cm^{-1}), the $\nu(CH_3)$ of generated CH_3OH (2963, 2853 cm^{-1}) and the $\nu(CH_3)$ of the metal cation site (2926 cm^{-1}, [M-CH_3]), respectively [24]. As noted, except for the band at 2926 cm^{-1} belonging to the $\nu(CH_3)$ of [M-CH_3], no obvious bands related to the $\nu(CH_3)$ of methoxy groups (CH_3O, 2980, 2869 and 2823 cm^{-1}) [27] can be observed, which implies that the H_2O-mediated N_2O DMTM follows the radical mechanism in which the CH_4 is activated into the radical of CH_3- and OH- at the evolved active site of [Fe-O-Cu] of $Fe_{0.6\%}Cu_{0.64\%}$-BEA. To further verify this assumption, in situ FTIR by introducing the CH_4 (2 vol% in He) into the N_2O-pretreated $Fe_{0.6\%}Cu_{0.64\%}$-BEA was further conducted, wherein the H_2O was not fed into the system to avoid its influence on ν(OH). As shown in Figure 5c, the band at 3675, being

related to the υ(OH) at metal cations site (α-site), can be clearly observed, which can solidly verify the deduction that the CH_4 activation would follow the radical mechanism over $Fe_{0.6\%}Cu_{0.64\%}$-BEA, as illustrated by Equations (1) and (2), wherein the M_a and M_b in Equation (2) represent the metal cations of Cu or Fe, respectively (the specific states will be determined by the DFT, as will be further discussed later).

$$N_2O + [Cu] - -[Fe] - Z \rightarrow [Cu - O - Fe] - Z + N_2 \quad (1)$$

$$CH_4 + [Cu - O - Fe] - Z \rightarrow [M_a - CH_3] - -[M_b - OH] - Z \quad (2)$$

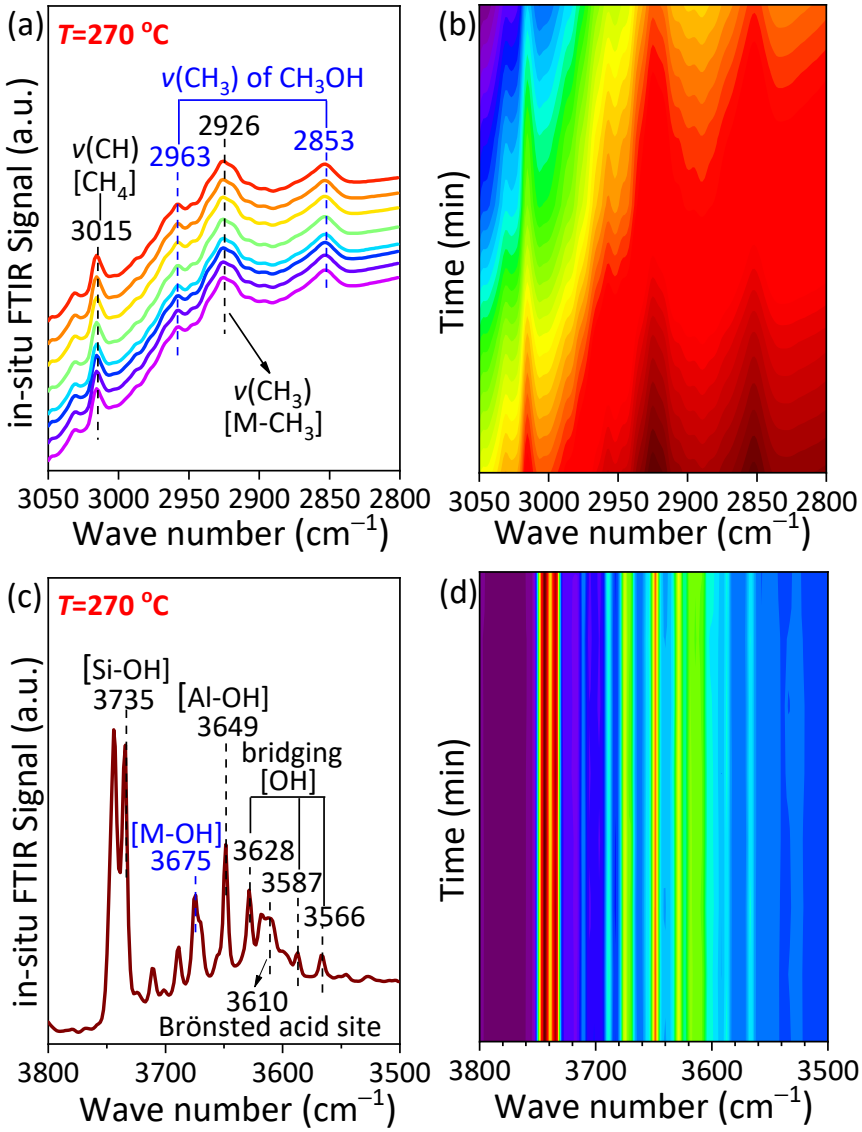

Figure 5. In situ FTIR spectra derived under different conditions over the $Fe_{0.60\%}Cu_{0.68\%}$-BEA: (**a**,**b**) co-feeding experiment of N_2O (2 vol%, in He), CH_4 (2 vol%, in He) and H_2O (bubbled by the mixed flow of 40 mL·min^{-1}) at a time interval of 0.5 min (T = 270 °C), wherein the sample was pretreated in situ for 1 h at T = 500 °C under vacuum conditions; (**c**,**d**) after the vacuum (T = 500 °C, 1 h) and subsequent N_2O (2 vol% in He, T = 270 °C of 1 h) pretreatment, the IR signal begins to be monitored along with the interaction with CH_4 (2 vol%, in He).

Therefore, based on the in situ FTIR, we can deduce that the neighboring [Fe]–[Cu] would initially interact with N_2O, generating [Fe-O-Cu] (α-site), which thereby favors CH_4 activation following a radical mechanism.

(b) D_2O isotopic tracer experiment

According to our previous study [24], the H_2O molecules could directly participate in N_2O DMTM through a proton-transfer route after the activation of CH_4 at the evolved [Cu-O-Cu] site of $Cu_{0.6\%}$-BEA. In light of that, the temperature-programmed surface reaction (TPSR-) MS-based D_2O isotopic tracer technique was also employed in the present work to explore whether the proton-transfer reaction of H_2O also occurs during the H_2O-mediated N_2O DMTM over the $Fe_{0.6\%}Cu_{0.68\%}$-BEA. As shown in Figure 6a, the obviously emerged peaks of CH_3OD (33) and D_3O^+ (33), accompanied by the simultaneous increase/decline in the signals of HOD (19)/[D_2O (20)], respectively, provide us with solid evidence that the D_2O can also participate in the N_2O DMTM through a proton-transfer route after CH_4 activation over the evolved [Fe-O-Cu] site of $Fe_{0.6\%}Cu_{0.68\%}$-BEA (see Equation (3)).

$$[M_a - CH_3] - -[M_b - OH] - Z + 2D_2O \xrightarrow[\text{Proton trasfer}]{D_3O^+} CH_3OD + HOD + D_2O + [M_a] - -[M_b] \quad (3)$$

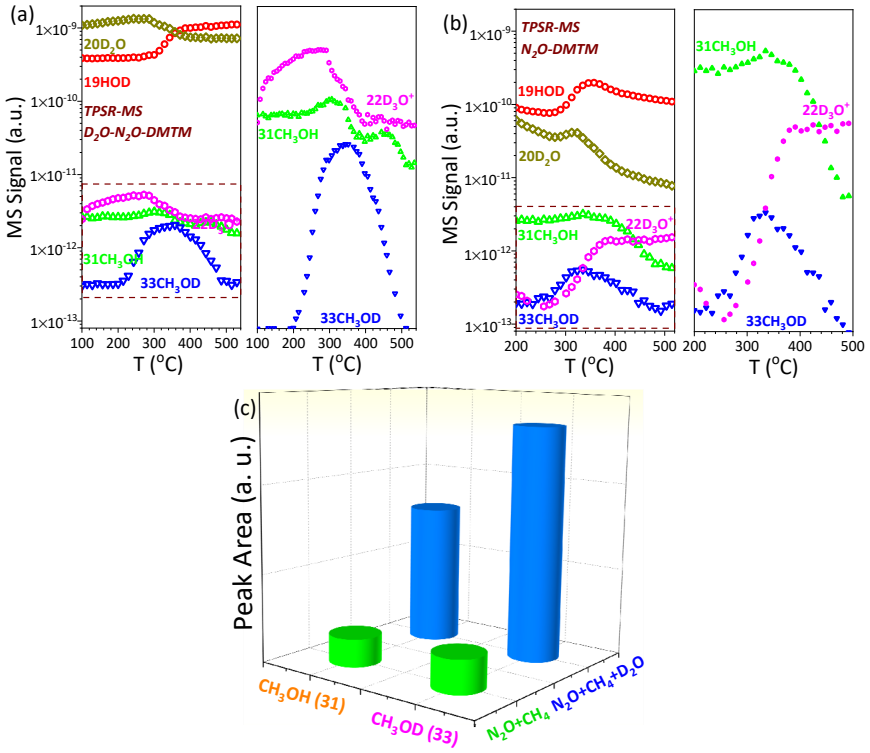

Figure 6. D_2O isotopic tracer study based on temperature-programmed surface reaction (TPSR) over the $Fe_{0.60\%}Cu_{0.68\%}$-BEA. (**a**) D_2O-mediated N_2O DMTM and (**b**) N_2O DMTM in the absence of D_2O; as noted, the signal contributions of CH_3OD (33), D_3O^+ (22), HOD (19) and D_2O (22) from panel (**b**) (N_2O DMTM without D_2O) have been subtracted from panel (**a**); (**c**) peak area comparisons of CH_3OH (31) and CH_3OD (33) derived in panels (**a**,**b**).

To make comparisons, the TPSR-MS without D_2O addition was also conducted over $Fe_{0.6\%}Cu_{0.68\%}$-BEA, as shown in Figure 6b. It is observed that the signals of CH_3OD (33), D_3O^+ (22), HOD (19) and D_2O (22) can also be detected, especially for D_2O (22), emerging as a small peak. In fact, this can be related to the overoxidation of CH_4 (99.999%), which contains small isotopic abundance of the atomic D, to produce minor D_2O that can further participate in the N_2O DMTM reaction following the proton-transfer route, eventually generating the detected signals of CH_3OD (33), HOD (19) and D_3O^+ (22) in Figure 6b. Therefore, this finding can also support the H_2O proton reaction during N_2O DMTM over $Fe_{0.6\%}Cu_{0.68\%}$-BEA.

Figure 3c further compares the peak areas of the signals of CH_3OH (31) and CH_3OD (33) derived from Figure 3a,b, which demonstrates that the addition of D_2O would lead to N_2O DMTM following the proton-transfer route by producing much higher amounts of CH_3OD (33) relative to that of CH_3OH (31). Small amounts of CH_3OH can also be generated during the D_2O-mediated N_2O DMTM, which may be related to the N_2O DMTM over the monomeric cation sites, where no proton-transfer reactions can occur [24]. In addition to that, herein, we suggest that the D_2O direct-reaction route may also exist during the D_2O-mediated N_2O DMTM, wherein one D_2O molecule can dissociatively react with the $[CuCH_3]$–[FeOH] to generate $[CuCH_3OD]$–[FeOHD] (see Equation (4)). This reaction route will be discussed later based on the DFT and with the results being further compared with that of the H_2O proton-transfer route.

$$D - O^aD + [CuCH_3] - -[FeOH] \rightarrow [CuCH_3O^aD] - -[FeOHD] \quad (4)$$

2.4.2. Theoretical Mechanism Simulations by DFT and AIMD

To shed deeper mechanistic insight into reaction synergy of the neighboring Fe and Cu cations of $Fe_{0.6\%}Cu_{0.68\%}$-BEA, both the DFT and AIMD were employed in this part to simulate the reaction mechanism based on the constructed FeCu-BEA model with the neighboring [Fe]–[Cu] as the active site (auto-reduced form after He pretreatment, see Figure S7). In total, three types of reaction mechanisms were proposed, including the H_2O absence mechanism (taken for comparison) and the H_2O proton-transfer mechanism as well as the H_2O direct-reaction mechanism, as illustrated in detail in in Scheme 1. The derived reaction energy diagrams are depicted in Figure 7a and Figure S8a,b, as stated in detail below.

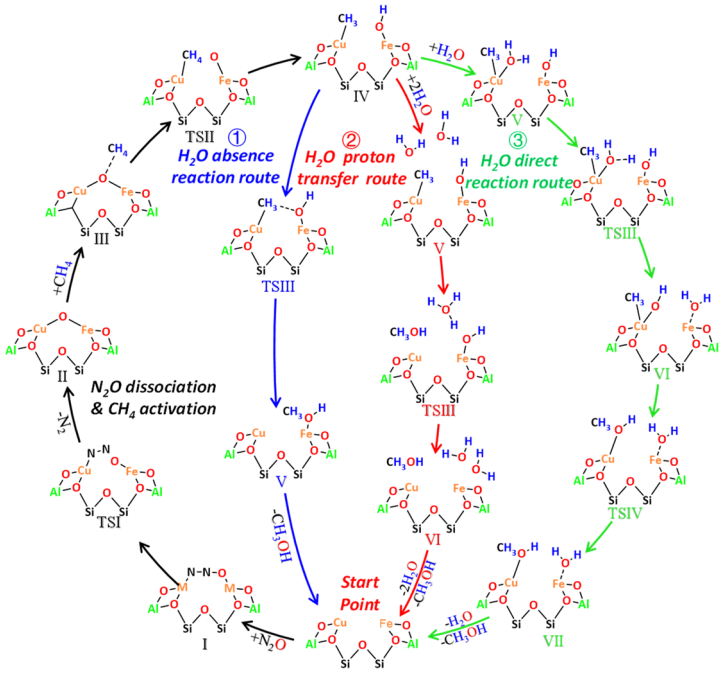

Scheme 1. Schematic diagram of proposed N_2O DMTM reaction mechanism over the best-performing sample of $Fe_{0.6\%}Cu_{0.68\%}$-BEA in the presence and absence of H_2O; specifically, after the initial N_2O dissociation and CH_4 activation steps (black line), three types of routes were proposed, namely: (i) in the absence of H_2O (blue line); (ii) the H_2O proton-transfer route (red line); and (iii) the H_2O direct-reaction route. The chemical structure was labeled according to constructed models depicted in the energy diagrams of Figure 7 and Figure S8a,b.

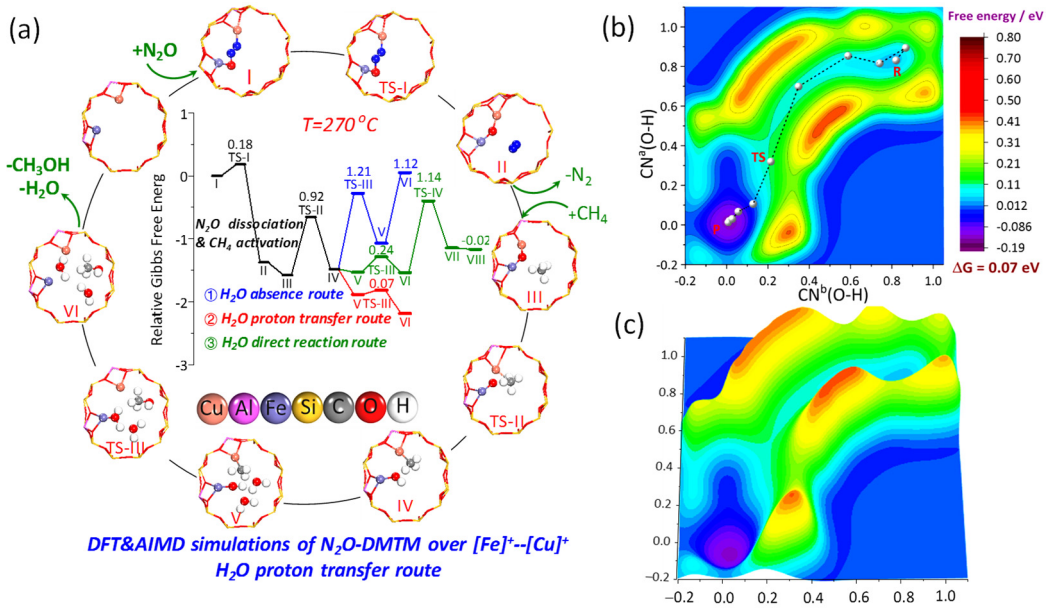

Figure 7. H_2O-mediated N_2O DMTM mechanism simulation results of the H_2O proton-transfer route over $Fe_{0.6\%}Cu_{0.68\%}$-BEA with the neighboring bimetallic cation active site of $[Fe]^+$–$[Cu]^+$, wherein the initial N_2O dissociation and CH_4 activation steps of (I→IV) were simulated by DFT, while the H_2O proton-transfer route (V→VI) was simulated by AIMD; (**a**) derived free energy diagram along with the reaction coordinate (with the unadsorbed reactant and desorbed product being taken into account to obtain the net change of the reaction energy); metadynamics-computed free energy surface in a (**b**) 2D and (**c**) 3D view based on the AIMD, wherein the minimal free energy route is shown by gray balls in panel (**b**).

(a) N_2O dissociation and CH_4 activation steps

As shown in Scheme 1, the same reaction routes are followed during the initial N_2O dissociation and CH_4 activation steps (marked by black arrow) for the three proposed types of mechanisms. Specifically, the N_2O molecule readily interacts with the neighboring [Fe]–[Cu] site to generate the α-site of [Fe-O-Cu] by overcoming an extremely low Gibbs free energy barrier of ΔG = 0.18 eV (see TS-I of Figure 7a), which is much lower than those derived from Cu-BEA of our previous work (ΔG = 0.91 and 1.31 eV of di-copper [Cu]–[Cu] site and monomeric [Cu] site, respectively) [24]. This finding demonstrates that the synergetic effect of the neighboring [Fe]–[Cu] could significantly promote N_2O dissociation to generate the active O, which constitutes the major reason leading to the much higher CH_3OH productivity and lower operation temperature of $Fe_{0.6\%}Cu_{0.68\%}$-BEA relative to that of $Cu_{0.6\%}$-BEA of our previous work. After that, the CH_4 can be subsequently activated into CH_3- and OH- (III→IV, Figure 7a); a similar reaction route of III→TSII has also been reported by the literature [35,36], following a radical mechanism as revealed by the in situ FTIR (Figure 5a–d), the free energy barrier of which is calculated to be 0.92 eV (TS-II of Figure 7a). Noteworthily, according to the DFT calculations (Figure S9a,b), the CH_4 is both kinetically and thermodynamically much more favorable to be activated into the [Fe-OH]–[Cu-CH_3] state relative to the scenario of the [Fe-CH_3]–[Cu-OH] state.

(b) Further reaction of [Fe-OH]–[Cu-CH_3] in the absence and presence of H_2O

H_2O absence mechanism. Three types of routes were proposed for the further reaction of [Fe-OH]–[Cu-CH_3]. As shown in Scheme 1 and Figure S8a, the H_2O absence route would follow the widely reported rebound mechanism, wherein the radical of CH_3- could migrate from the $[Cu]^{2+}$ site to interact with OH-, producing [Fe(CH_3OH)] (IV→V) by overcoming a relatively high free energy barrier of 1.21 eV (TS-III). After crossing another energy barrier of 1.12 eV (VI), the CH_3OH can be eventually desorbed.

H_2O proton-transfer mechanism. Based on the above in situ FTIR (Figure 5a–d) and D_2O isotopic transfer (Figure 6a,b) studies, the AIMD-based metadynamic simulations were employed to explore the H_2O proton-transfer mechanism (see Movie S1, T = 270 °C, *P* = 1 atm). As shown in Figure 7a, two H_2O molecules can be initially inserted between the generated radicals of [FeOH]–[$CuCH_3$] (model V), which is much more thermodynamically favorable than the scenario of the H_2O direct-reaction mechanism with one H_2O molecule being adsorbed on the $[Cu]^{2+}$ site (as will be further discussed later). After that, one H_2O molecule would dissociatively interact with the neighboring [$CuCH_3$] and H_2O molecule to produce $[CuCH_3OH]^+$ and H_3O^+, respectively (as detected by means of the D_2O isotopic transfer technique in Figure 6a). Subsequently, one H^+ could quickly migrate from the H_3O^+ to [FeOH], generating $[FeOH_2]^+$ (adsorbed H_2O), and the H_3O^+ would be restored to H_2O. Finally, the adsorbed CH_3OH and H_2O ([$CuCH_3OH$]–[$FeOH_2$]) could be barrierlessly desorbed to regenerate the [Fe]–[Cu] active site. Noteworthily, an extremely low energy barrier of 0.07 eV can be observed during the H_2O proton-transfer process, which is comparable to the value of 0.03 and 0.05 eV for the scenario of $Cu_{0.6\%}$-BEA presented in our previous work [24]. This finding validates the suggestion that the synergistic effect of the neighboring [Fe]–[Cu] site can also favor the H_2O proton-transfer reaction to pronouncedly promote CH_3OH productivity over $Fe_{0.6\%}Cu_{0.68\%}$-BEA, as observed in Figure 2a. The Gibbs free energy surface is further depicted in Figure 7b,c as a function of the coordinate number of CN^a(O-H) and CN^b(O-H) (see Figure S1a), which clearly displays the reaction energy variations from one energy minimum to another minimum.

H_2O direct-reaction mechanism. As stated above, the H_2O direct-reaction route may also occur during the H_2O-mediated DMTM over $Fe_{0.6\%}Cu_{0.68\%}$-BEA. In this regard, the H_2O direct-reaction mechanism was further simulated by DFT. As shown in Figure S8b, initially, one H_2O site forms $[H_2OCuCH_3]^+$ (VII). Thereby, the H_2O can be readily dissociated from (H-^{a}O^{a}H) to react with the [FeOH] and [Cu-CH_3], producing [$FeOH_2$]–[^{a}H^{a}O$CuCH_3$] (ΔG = 0.24 eV, TS-III). After the rebounding of CH_3- and ^{a}O^{a}H- by crossing a free energy barrier of ΔG = 1.14 eV (TS-V), [$CuCH_3{}^aO^aH$] can be formed. With the assistance of H_2O (being desorbed from [$FeOH_2$]), the $CH_3{}^aO^aH$ can be barrierlessly released from the $[Cu]^{2+}$ site.

(c) Reaction mechanism comparisons

In comparison to the H_2O absence mechanism, the slightly lower barrier of the radical rebound step (1.14 (TSIV, marked blue) versus 1.21 eV (TSIII, marked green) (see inserted energy diagram of Figure 7a) combined with the barrierless desorption of CH_3OH indicates that H_2O could also favor CH_3OH production through the direct-reaction route. However, the H_2O-mediated N_2O DMTM would generally follow the H_2O proton-transfer route due to the extremely low energy barrier of 0.07 eV. To make quantitative comparisons, microkinetic modeling was further conducted for these three types of mechanisms, with the results being profiled in Figure S10a–d. As can be seen (Figure S10a), the overall reaction rates were predicted to be 3.64×10^9 s^{-1} (H_2O proton-transfer route), 1.05×10^4 s^{-1} (H_2O direct-reaction route) and 7.64×10^{-10} s^{-1} (H_2O absence route), respectively, which quantitatively verified that the significant promotion effect of H_2O during N_2O DMTM is generally through the H_2O proton-transfer route, being favored by the synergistic effect of the neighboring [Fe]–[Cu] site. It is worth noting that the DFT-calculated reaction rate of the H_2O-mediated N_2O DMTM was several orders of magnitude higher than that of the H_2O-absence N_2O DMTM; however, it was only two times higher for the scenario of the experimental result of Figure 2a (CH_3OH productivity). This discrepancy is related to the utilized DFT calculation method during the microkinetic modeling, especially for the pre-exponential factor calculations derived by the frequency calculations. However, it does not affect the parallel comparisons of the DFT-based microkinetic modeling results.

2.4.3. Illustration of the Synergistic Effect of Neighboring Fe and Cu Cations

Based on the above experimental and theoretical mechanism studies, we can obtain a comprehensive understanding of the synergistic effect of the neighboring [Fe]–[Cu] cations

during the H_2O-mediated N_2O DMTM. On the one hand, it can efficiently promote N_2O dissociation to generate active O ([Fe-O-Cu]) by extensively reducing the N_2O dissociation barrier from 0.91 eV (the neighboring [Cu]–[Cu] site [24]) to 0.18 eV. On the other hand, it can also motivate the reaction following the H_2O proton-transfer route by crossing an extremely low free energy barrier of 0.07 eV, thereby pronouncedly enhancing CH_3OH productivity/selectivity, as well as long-term stability (reducing carbon depositions). To provide deeper insights, from the electronic structure point of view, into the synergistic effect of neighboring [Fe]–[Cu] on N_2O dissociation to generate active O, the theoretical simulations including electronic density difference, the Bader charge analysis and density of state (DOS) were further conducted (see Figure 8a–d) based on the optimized N_2O-adsorption model and DFT, wherein the neighboring [Cu]–[Cu] was also taken into account for comparison.

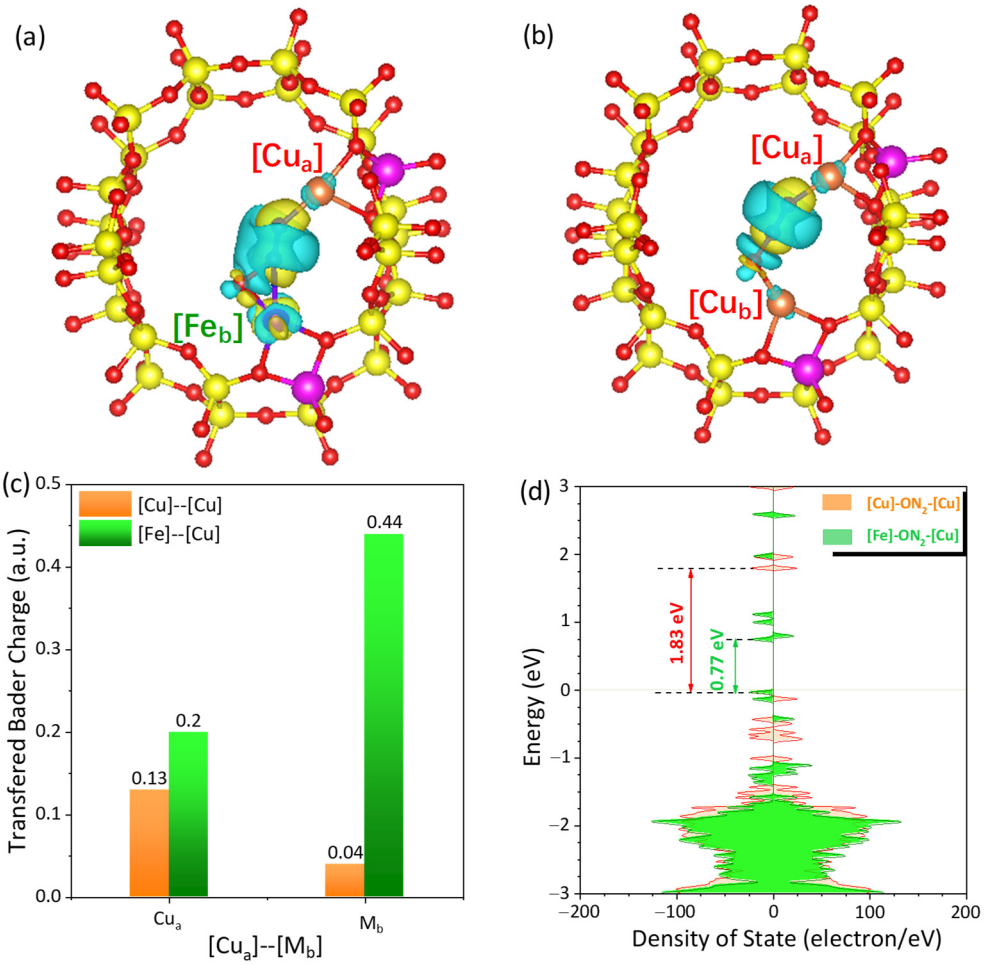

Figure 8. (**a**,**b**) Electronic density difference upon adsorption of N_2O onto FeCu-BEA and Cu-BEA, respectively, with neighboring [Fe]–[Cu] and [Cu]–[Cu] as the active site; the yellow and blue colors represent electron density increases and decreases, respectively; the metal cations are labeled by the subscript characters a and b to mark differences; (**c**) comparisons of transferred charges after adsorption of N_2O for the neighboring metal cations based on the Bader charge analysis; (**d**) total DOS comparisons for the models depicted in panels (**a**,**b**); Si (yellow), O (red), N (blue), Al (pink), Cu (orange) and Fe (purple).

As can be seen (Figure 8a,b), much higher amounts of charge transfers occur after the adsorption of N_2O onto the the [Fe]–[Cu] site, wherein the bimetal cations of [Fe]–[Cu], especially for the cationic [Fe], acting as the charge donors, donate much greater charges (0.2 and 0.44) to the N_2O molecule relative to that of the neighboring [Cu]–[Cu] cations

(0.13 and 0.04, see Figure 8c). This finding indicates that the neighboring [Fe]–[Cu] site can exert much a stronger electric field effect on the adsorbed N_2O, which is greatly favorable for the pre-activation of N_2O and subsequent O-N_2 bond fracture to produce active O. As observed (Figure S11a,b), much more extensive structure distortion can be clearly observed for the adsorbed N_2O molecule onto the [Fe]–[Cu] site: ∠N-N-O bending from 180° to 129.7° versus (180° → 175°) of the [Cu]–[Cu] site. The stronger charge transfer effect (or electric filed effect) of the [Fe]–[Cu] site can be explained by the total DOS (Figure 8d) as well as partial DOS (PDOS) results (Figure S12a–h), which indicates that the [Fe]–[Cu] site not only possesses much lower electron-transfer band gaps but also can reduce the band gaps of the N and O atoms, N_2O (0.77 versus 1.83 eV), eventually significantly promoting the charge transfers between the [Fe]–[Cu] active site and the N_2O molecule. In light of the above studies, we can conclude that the much more efficient synergistic effect of the [Fe]–[Cu] active site (relative to that of [Cu]–[Cu] site) during the N_2O dissociation step can be interpreted by its stronger electric field effect, leading to the significantly enhanced electron transfer between the bimetal active site and the N_2O molecule due to the lowered band gaps of bimetal cations as well as the N and O atoms of the N_2O molecule.

3. Materials and Methods

3.1. Experimental Methods

3.1.1. Catalyst Preparation

The commercial H-BEA with the Si/Al of 12.5 (mole ratio) was purchased from Tianjin Nankai University Catalyst Co., Ltd. of China, based on which a series of Fe_nCu_m-BEA zeolites (Table S1) were prepared by means of the traditional wet ion-exchange method. For the purpose of comparison, the monomeric $Fe_{1.28\%}$- and $Cu_{1.28\%}$-BEA, with the total metal loading amounts being the same as those of $Fe_{0.6\%}Cu_{0.68\%}$-BEA (1.28 wt.%), were prepared by means of an incipient-wetness impregnation method. More details regarding the catalytic preparations are stated in the Supplementary Materials.

3.1.2. Catalyst Characterizations

The characterizations of X-ray diffraction (XRD), element content (determined by inductively coupled plasma (ICP), X-ray photoelectron spectroscopy (XPS), N_2 adsorption/desorption, H_2-temperature programmed reduction (H_2-TPR), UV-vis diffuse-reflectance, in situ FTIR and D_2O isotopic tracer were conducted as described in detail in our previous work [24]—alternatively, please see details in the Supplementary Materials.

3.1.3. Activity Measurement

The continuous N_2O DMTM in both scenarios of the presence and absence of H_2O (10 vol%) was conducted over a fixed bed reactor (O.D. 11 mm, I.D. 8 mm, L485 mm) under a total flow rate of 100 mL· min^{-1} [GHSV (gas hourly space velocity) = 12,000 h^{-1}]. The reaction products were analyzed by a gas chromatograph (SHIMADZU GC-2014) being equipped with the thermal conductivity detector (TCD) and flame ionization detector (FID). To prevent condensation, the gas line from the point of liquid injection to then GC unit was heated (T = 200 °C) by resistive heating tape. More details regarding activity measurement can be found in the Supplementary Materials or our previous work [24].

3.2. Computational Methods

3.2.1. Constructed Model

The model of Fe_nCu_m-BEA with the neighboring [Fe]–[Cu] bimetal active site was constructed based on the BEA structure (a = 12.632, b = 12.632 and c = 9.421 Å) from the database of IZA [37], wherein the framework Al was located at the T2 and T5 site according to our previous work [24], and the Si atoms were set to be fixed during the structure optimization and transition state (TS) calculations to keep the structure of BEA.

3.2.2. Computational Method

The periodic density functional theory (DFT) analysis was performed based on the Vienna ab-initio simulation package (VASP) [38], which was employed in the present work to simulate the N_2O DMTM mechanism (in the presence and absence of H_2O) and conduct microkinetic analysis, electronic structure analysis (including electronic density difference, Bader charge and density of state (DOS)) and ab initio thermodynamics analysis (evaluating the thermostabilities of active-site motif and generating radical intermediate). The ab initio molecular dynamics (AIMD) analysis was conducted based on CP2K code [39] to explore the H_2O proton-transfer mechanism, wherein the AIMD-based metadynamic simulations were conducted utilizing two types of collective variables, the coordination numbers (CN) of [CN^aO-H] and [CN^bO-H] (as illustrated in Figure S1a). The detailed method descriptions of DFT and CP2K can be found in the Supplementary Materials or our previous work [24].

4. Conclusions

The present work systematically investigated the H_2O-mediated continuous N_2O DMTM over a series of Fe_nCu_m-BEA zeolites based on combined experimental and theoretical approaches. The strikingly promoted CH_3OH productivity (259.1 $\mu mol \cdot g^{-1}_{cat} \cdot h^{-1}$) and selectivity (71.7%), as well as long-term reaction stability, can be achieved over the best-performed sample of $Fe_{0.6\%}Cu_{0.68\%}$-BEA, which is closely correlated with the synergistic effect of the loaded neighboring Fe and Cu cations. On the one hand, it is much more favorable for N_2O dissociation to generate the αO (bridge O of $[Fe\text{-}O\text{-}Cu]^{2+}$, ΔG = 0.18 eV at T = 270 °C) due to the exerted strong electric field effect. On the other hand, it can motivate the N_2O DMTM reaction following a H_2O-mediated proton-transfer route to produce CH_3OH by crossing a much lower energy barrier (ΔG = 0.07 eV), eventually pronouncedly enhancing CH_3OH production and desorption as well as the catalytic reaction's long-term stability (through efficiently reducing carbon depositions). Generally, the present work reported the synergistic effect of neighboring Fe and Cu cations over the Fe_nC_m-BEA zeolite, which can efficiently promote its CH_3OH productivity/selectivity during H_2O-mediated N_2O DMTM. Thereby, employing the synergistic effect of bimetallic cations to modify zeolitic activity constitutes a promising strategy for a highly efficient catalyst design for the DMTM.

Supplementary Materials: The following are available online at https://www.mdpi.com/article/10.3390/catal11121444/s1: Figure S1: (a) Illustration of selected coordination number (CN) during the AMID-based metadynamic simulations: $CN^a_{(O\text{-}H)}$ (red dash line) and $CN^b_{(O\text{-}OH)}$ (green dash line) respectively represent the O-H bond of H_2O molecules; $CN^c_{(O\text{-}H)}$ (blue arrow) and $CN^d_{(O\text{-}H)}$ (pink arrow) respectively represent the to be generate O-H bond of H_3O^+ and H_2O (over the Fe site); (b) variations of derived CN numbers indicating (O-H) bond factures the H_2O molecule to follow the H_2O-proton-transfer reaction at t < 50 fs, Figure S2: (a) X-ray diffraction patters and (b) isothermal adsorption curves (derived by N_2 adsorption/desorption) of Fe_nCu_m-BEA and monomeric $Fe_{1.28\%}$- and $Cu_{1.28\%}$-BEA; (c) TEM-EDX mapping results of $Fe_{0.6\%}Cu_{0.68\%}$-BEA-0.6% (the Fe and Cu species are uniformly distributed on the catalyst), Figure S3: XPS characterization results of (a) $Fe_{1.28\%}$- and (b) $Cu_{1.28\%}$-BEA (the metal cations constitute major metallic species). Figure S4: Activity measurement results of N_2O-DMTM in both presence and absence of H_2O over the prepared bimetallic Fe_nCu_m-BEA and monomeric $Fe_{1.28\%}$-, $Cu_{1.28\%}$-BEA samples after 5 h's reactions: (a) CH_3OH productivity; (b) product selectivity; (c) CH_4 conversion; (d) N_2O conversion; reaction condition N_2O:CH_4:H_2O:He = 30:15:10:45 (presence of H_2O); and O_2:CH_4:He = 30:15:55 (absence of H_2O); GHSV = 12,000 h^{-1} and T = 270 °C, Figure S5: (a) UV-vis spectra of $Fe_{0.6\%}Cu_{0.68\%}$-BEA being respectively pretreated by N_2O at T = 200, 250 and 300 °C; no obvious band emerged at 440 nm belong to the characteristic peak of [Cu-O-Cu]; (b) thermodynamic stabilities comparisons of diverse bimetallic active sites, including [Cu-O-Cu], [Fe-O-Cu] and [Fe-O-Fe] based on the DFT-based *ab initio* thermodynamic analysis by taking the reaction condition of present work into account: 10 vol% H_2O, 30 vol% N_2O, and total pressure of 1 atm; obviously, the [Fe-O-Cu] & [Cu-O-Cu] possessed much lower formation Gibbs free energy than that of $[Fe\text{-}O\text{-}Fe]^{2+}$ site, indicating higher thermodynamic

stability; as noted, the data of ΔG for [Cu-O-Cu]-Z was covered by those of [Fe-O-Cu]-Z, Figure S6: O_2-DMTM activity measurement result over Fe0.6%Cu0.68%-BEA with the reaction condition being similar to that of N_2O-DMTM:O_2:CH_4:H_2O:He = 30:15:10:45, GHSV = 12,000 h^{-1} and T = 270 °C, Figure S7: Optimized periodic FeCu-BEA model with neighboring [Fe]–[Cu] as the active site, Figure S8: (a) DFT simulated H_2O absence mechanism during N_2O-DMTM over construed Fe_nCu_m-BEA model with neighboring [Fe]–[Cu] as the active site, (b) DFT simulated H_2O direct reaction mechanism during N_2O-DMTM over construed Fe_nCu_m-BEA model with the neighboring [Fe]–[Cu] as active site with the derived Gibbs free energy being compared with that of H_2O absence mechanism (see inserted energy diagram), Figure S9: (a) kinetic comparisons of radical evolutions during CH_4 activation step; (b) thermostability comparisons of generated intermediate radicals in [$FeCH_3$]–[CuOH] and [FeOH]–[$CuCH_3$] state based on ab initio thermodynamics taking the reaction conditions of 10 vol% H_2O, 30 vol% N_2O and 1 atm into account, Figure S10: Microkinetic modeling results based on DFT at T = 270 °C: (a) overall reaction rate of different reaction mechanisms; surface coverage variations as a function of reaction time *t* of (b) H_2O absence route; (c) H_2O direct reaction route; and (d) H_2O proton transfer reaction route. Figure S11: Optimized N_2O-adsorption model of with (a) neighboring [Fe]–[Cu] site and (b) neighboring [Cu]–[Cu] site; Si (yellow), O (red), N (blue), Al (pink), Cu (orange) and Fe (purple), Figure S12: Partial density of sate (PDOS) of bimetal cations and N, O atoms of N_2O based on N_2O-adsorption models; (a–d) [Fe_b], [Cu_a], atomic O and end N of N_2O over neighboring [Fe]–[Cu] model; (e–h) [Cu_b], [Cu_a], atomic O and end N of N_2O over neighboring [Cu]–[Cu] model, Figure S13: Reaction condition determination based on the N_2O-DMTM measurement over $Fe_{0.6\%}Cu_{0.68\%}$-BEA: (a) reaction temperature (T); (b) introduced H_2O content, Figure S14: N_2O-DMTM activity measurement result over Fe_nCu_m-BEA and monomeric $Fe_{1.28\%}$-, $Cu_{1.28\%}$-BEA in presence (a–b) and absence (c–d) of H_2O for 5 h: (a,c) CH_3OH productivity; (b,d) N_2O conversion, Figure S15: Thermogravimetry (TG) and differential thermogravimetric analysis (DTG) curves of the $Fe_{0.6\%}Cu_{0.68\%}$-BEA-0.6% samples being after 25 h's long-term test in absence (a) and presence (b) of 10vol% H_2O, Figure S16: ^{29}Si MAS NMR of $Fe_{0.6\%}Cu_{0.68\%}$-BEA being respectively before and after the 5 h's reaction (H_2O-mediated N_2O-DMTM), Table S1: Physicochemical property of investigated samples, Table S2: Consumption of metal salts for catalysts preparation, Table S3: Loaded Fe and Cu species quantifications based on H_2-TPR, Table S4: Methane conversion and products selectivity of investigated samples, Table S5: (a) Elementary steps and kinetic parameters involved in microkinetic modeling for the H_2O absence mechanism, (b) Elementary steps and kinetic parameters involved in microkinetic modeling for the H_2O direct reaction mechanism, (c) Elementary steps and kinetic parameters involved in microkinetic modeling for the H_2O-proton-transer mechanism. Movie S1: AIMD-based metadynamics simulation of H_2O-mediated proton transfer route during N_2O-DMTM over FenCum-BEA.

Author Contributions: Conceptualization, N.L.; methodology, Y.L.; validation, C.D.; investigation, Y.L.; resources, B.C.; data curation, R.X.; writing—original draft preparation, Y.L.; writing—review and editing, N.L.; visualization, G.Y.; supervision, B.C.; project administration, N.W.; funding acquisition, J.Z. All authors have read and agreed to the published version of the manuscript.

Funding: This research was funded by the National Key Research and Development Program of China (Projects: 2017YFC0210905) and National Natural Science Foundation of China (No. 21906003).

Data Availability Statement: Data is available upon request to the corresponding authors.

Acknowledgments: We acknowledge the final support from the National Key Research and Development Program of China (Projects: 2017YFC0210905) and National Natural Science Foundation of China (No. 21906003).

Conflicts of Interest: The authors declare no conflict of interest.

References

1. Agarwal, N.; Freakley, S.J.; McVicker, R.U.; Althahban, S.M.; Dimitratos, N.; He, Q.; Morgan, D.J.; Jenkins, R.L.; Willock, D.J.; Taylor, S.H.; et al. Aqueous Au-Pd colloids catalyze selective CH_4 oxidation to CH_3OH with O_2 under mild conditions. *Science* **2017**, *358*, 223–227. [CrossRef] [PubMed]
2. Luo, L.; Luo, J.; Li, H.; Ren, F.; Zhang, Y.; Liu, A.; Li, W.-X.; Zeng, J. Water enables mild oxidation of methane to methanol on gold single-atom catalysts. *Nat. Commun.* **2021**, *12*, 1218. [CrossRef] [PubMed]
3. Ravi, M.; Ranocchiari, M.; Van Bokhoven, J.A. The Direct Catalytic Oxidation of Methane to Methanol-A Critical Assessment. *Angew. Chem. Int. Ed.* **2017**, *56*, 16464–16483. [CrossRef]

4. Li, M.; Shan, J.; Giannakakis, G.; Ouyang, M.; Cao, S.; Lee, S.; Allard, L.F.; Flytzani-Stephanopoulos, M. Single-step selective oxidation of methane to methanol in the aqueous phase on iridium-based catalysts. *Appl. Catal. B Environ.* **2021**, *292*, 120124. [CrossRef]
5. Kulkarni, A.R.; Zhao, Z.-J.; Siahrostami, S.; Nørskov, J.K.; Studt, F. Monocopper Active Site for Partial Methane Oxidation in Cu-Exchanged 8MR Zeolites. *ACS Catal.* **2016**, *6*, 6531–6536. [CrossRef]
6. Dinh, K.T.; Sullivan, M.; Serna, P.; Meyer, R.J.; Dincă, M.; Román-Leshkov, Y. Viewpoint on the Partial Oxidation of Methane to Methanol Using Cu- and Fe-Exchanged Zeolites. *ACS Catal.* **2018**, *8*, 8306–8313. [CrossRef]
7. Jeong, Y.R.; Jung, H.; Kang, J.; Han, J.W.; Park, E.D. Continuous Synthesis of Methanol from Methane and Steam over Copper-Mordenite. *ACS Catal.* **2021**, *11*, 1065–1070. [CrossRef]
8. Hammond, C.; Forde, M.; Ab Rahim, M.H.; Thetford, A.; He, Q.; Jenkins, R.L.; Dimitratos, N.; Lopez-Sanchez, J.A.; Dummer, N.; Murphy, D.; et al. Direct Catalytic Conversion of Methane to Methanol in an Aqueous Medium by using Copper-Promoted Fe-ZSM-5. *Angew. Chem. Int. Ed.* **2012**, *51*, 5129–5133. [CrossRef]
9. Hammond, C.; Dimitratos, N.; Jenkins, R.L.; Lopez-Sanchez, J.A.; Kondrat, S.A.; ab Rahim, M.H.; Forde, M.M.; Thetford, A.; Taylor, S.H.; Hagen, H.; et al. Elucidation and Evolution of the Active Component within Cu/Fe/ZSM-5 for Catalytic Methane Oxidation: From Synthesis to Catalysis. *ACS Catal.* **2013**, *3*, 689–699. [CrossRef]
10. Xu, J.; Armstrong, R.D.; Shaw, G.; Dummer, N.; Freakley, S.; Taylor, S.H.; Hutchings, G.J. Continuous selective oxidation of methane to methanol over Cu- and Fe-modified ZSM-5 catalysts in a flow reactor. *Catal. Today* **2016**, *270*, 93–100. [CrossRef]
11. Yu, T.; Li, Z.; Lin, L.; Chu, S.; Su, Y.; Song, W.; Wang, A.; Weckhuysen, B.M.; Luo, W. Highly Selective Oxidation of Methane into Methanol over Cu-Promoted Monomeric Fe/ZSM-5. *ACS Catal.* **2021**, *11*, 6684–6691. [CrossRef]
12. Wang, L.; Li, Z.; Wang, Z.; Chen, X.; Song, W.; Zhao, Z.; Wei, Y.; Zhang, X. Hetero-Metallic Active Sites in Omega (MAZ) Zeolite-Catalyzed Methane Partial Oxidation: A DFT Study. *Ind. Eng. Chem. Res.* **2021**, *60*, 2400–2409. [CrossRef]
13. Dandu, N.K.; Adeyiga, O.; Panthi, D.; Bird, S.A.; Odoh, S.O. Performance of density functional theory for describing hetero-metallic active-site motifs for methane-to-methanol conversion in metal-exchanged zeolites. *J. Comput. Chem.* **2018**, *39*, 2667–2678. [CrossRef] [PubMed]
14. Wang, G.; Huang, L.; Chen, W.; Zhou, J.; Zheng, A. Rationally designing mixed Cu–(μ-O)–M (M = Cu, Ag, Zn, Au) centers over zeolite materials with high catalytic activity towards methane activation. *Phys. Chem. Chem. Phys.* **2018**, *20*, 26522–26531. [CrossRef] [PubMed]
15. Sazama, P.; Moravkova, J.; Sklenak, S.; Vondrova, A.; Tabor, E.; Sadovska, G.; Pilar, R. Effect of the Nuclearity and Coordination of Cu and Fe Sites in β Zeolites on the Oxidation of Hydrocarbons. *ACS Catal.* **2020**, *10*, 3984–4002. [CrossRef]
16. Tang, X.; Wang, L.; Yang, B.; Fei, C.; Yao, T.; Liu, W.; Lou, Y.; Dai, Q.; Cai, Y.; Cao, X.-M.; et al. Direct oxidation of methane to oxygenates on supported single Cu atom catalyst. *Appl. Catal. B Environ.* **2021**, *285*, 119827. [CrossRef]
17. Zhang, R.; Liu, N.; Lei, Z.; Chen, B. Selective Transformation of Various Nitrogen-Containing Exhaust Gases toward N2 over Zeolite Catalysts. *Chem. Rev.* **2016**, *116*, 3658–3721. [CrossRef] [PubMed]
18. Liu, N.; Zhang, R.; Chen, B.; Li, Y.; Li, Y. Comparative study on the direct decomposition of nitrous oxide over M (Fe, Co, Cu)–BEA zeolites. *J. Catal.* **2012**, *294*, 99–112. [CrossRef]
19. Zhao, G.; Benhelal, E.; Adesina, A.A.; Kennedy, E.M.; Stockenhuber, M. Comparison of Direct, Selective Oxidation of Methane by N2O over Fe-ZSM-5, Fe-Beta, and Fe-FER Catalysts. *J. Phys. Chem. C* **2019**, *123*, 27436–27447. [CrossRef]
20. Zhao, G.; Adesina, A.A.; Kennedy, E.M.; Stockenhuber, M. Formation of Surface Oxygen Species and the Conversion of Methane to Value-Added Products with N_2O as Oxidant over Fe-Ferrierite Catalysts. *ACS Catal.* **2020**, *10*, 1406–1416. [CrossRef]
21. Parfenov, M.V.; Starokon, E.V.; Pirutko, L.V.; Panov, G.I. Quasicatalytic and catalytic oxidation of methane to methanol by nitrous oxide over FeZSM-5 zeolite. *J. Catal.* **2014**, *318*, 14–21. [CrossRef]
22. Fan, L.; Cheng, D.-G.; Song, L.; Chen, F.; Zhan, X. Direct conversion of CH_4 to oxy-organics by N_2O using freeze-drying FeZSM-5. *Chem. Eng. J.* **2019**, *369*, 522–528. [CrossRef]
23. Ipek, B.; Lobo, R.F. Catalytic conversion of methane to methanol on Cu-SSZ-13 using N2O as oxidant. *Chem. Commun.* **2016**, *52*, 13401–13404. [CrossRef]
24. Xu, R.; Liu, N.; Dai, C.; Li, Y.; Zhang, J.; Wu, B.; Yu, G.; Chen, B. H_2O-Built Proton Transfer Bridge Enhances Continuous Methane Oxidation to Methanol over Cu-BEA Zeolite. *Angew. Chem. Int. Ed.* **2021**, *60*, 16634–16640. [CrossRef] [PubMed]
25. Memioglu, O.; Ipek, B. A potential catalyst for continuous methane partial oxidation to methanol using N_2O: Cu-SSZ-39. *Chem. Commun.* **2020**, *57*, 1364–1367. [CrossRef]
26. Narsimhan, K.; Iyoki, K.; Dinh, K.; Román-Leshkov, Y. Catalytic Oxidation of Methane into Methanol over Copper-Exchanged Zeolites with Oxygen at Low Temperature. *ACS Cent. Sci.* **2016**, *2*, 424–429. [CrossRef]
27. Sushkevich, V.L.; Palagin, D.; Ranocchiari, M.; Van Bokhoven, J.A. Selective anaerobic oxidation of methane enables direct synthesis of methanol. *Science* **2017**, *356*, 523–527. [CrossRef] [PubMed]
28. Palagin, D.; Sushkevich, V.L.; van Bokhoven, J.A. Water Molecules Facilitate Hydrogen Release in Anaerobic Oxidation of Methane to Methanol over Cu/Mordenite. *ACS Catal.* **2019**, *9*, 10365–10374. [CrossRef]
29. Liu, Z.; Huang, E.; Orozco, I.; Liao, W.; Palomino, R.M.; Rui, N.; Duchoň, T.; Nemšák, S.; Grinter, D.C.; Mahapatra, M.; et al. Water-promoted interfacial pathways in methane oxidation to methanol on a CeO 2 -Cu 2 O catalyst. *Science* **2020**, *368*, 513–517. [CrossRef] [PubMed]

30. Wu, Y.; Zhang, H.; Yan, Y. High efficiency of phenol oxidation in a structured fixed bed over Cu-ZSM-5/PSSF prepared by ion-exchanged method. *Chem. Eng. J.* **2020**, *380*, 122466. [CrossRef]
31. Xia, Y.; Zhan, W.; Guo, Y.; Guo, Y.; Lu, G. Fe-Beta zeolite for selective catalytic reduction of NOx with NH_3: Influence of Fe content. *Chin. J. Catal.* **2016**, *37*, 2069–2078. [CrossRef]
32. Xiao, P.; Osuga, R.; Wang, Y.; Kondo, J.N.; Yokoi, T. Bimetallic Fe–Cu/beta zeolite catalysts for direct hydroxylation of benzene to phenol: Effect of the sequence of ion exchange for Fe and Cu cations. *Catal. Sci. Technol.* **2020**, *10*, 6977–6986. [CrossRef]
33. Gao, F.; Kollar, M.; Kukkadapu, R.K.; Washton, N.M.; Wang, Y.; Szanyi, J.; Peden, C.H. Fe/SSZ-13 as an NH3-SCR catalyst: A reaction kinetics and FTIR/Mössbauer spectroscopic study. *Appl. Catal. B Environ.* **2015**, *164*, 407–419. [CrossRef]
34. Berlier, G.; Lamberti, C.; Rivallan, M.; Mul, G. Characterization of Fe sites in Fe-zeolites by FTIR spectroscopy of adsorbed NO: Are the spectra obtained in static vacuum and dynamic flow set-ups comparable? *Phys. Chem. Chem. Phys.* **2010**, *12*, 358–364. [CrossRef]
35. He, M.; Zhang, J.; Sun, X.-L.; Chen, B.-H.; Wang, Y.-G. Theoretical Study on Methane Oxidation Catalyzed by Fe/ZSM-5: The Significant Role of Water on Binuclear Iron Active Sites. *J. Phys. Chem. C* **2016**, *120*, 27422–27429. [CrossRef]
36. Mahyuddin, M.H.; Staykov, A.; Shiota, Y.; Yoshizawa, K. Direct Conversion of Methane to Methanol by Metal-Exchanged ZSM-5 Zeolite (Metal = Fe, Co, Ni, Cu). *ACS Catal.* **2016**, *6*, 8321–8331. [CrossRef]
37. Available online: http://www.iza-structure.org/databases/ (accessed on 5 November 2021).
38. Kresse, G.; Furthmüller, J. Efficient iterative schemes for ab initio total-energy calculations using a plane-wave basis set. *Phys. Rev. B* **1996**, *54*, 11169–11186. [CrossRef]
39. Hutter, J.; Iannuzzi, M.; Schiffmann, F.; VandeVondele, J. cp2k: Atomistic simulations of condensed matter systems. *WIREs Comput. Mol. Sci.* **2014**, *4*, 15–25. [CrossRef]